

Characterization of the Morphometry of Impact Craters Hosting Polar Deposits in
Mercury's North Polar Region

Matthieu J. Talpe¹, Maria T. Zuber¹, Di Yang¹, Gregory A. Neumann², Sean C.
Solomon^{3,4}, Erwan Mazarico^{1,2}, Faith Vilas⁵

¹Department of Earth, Atmospheric and Planetary Sciences, Massachusetts Institute of
Technology, Cambridge, Massachusetts, USA.

²NASA Goddard Space Flight Center, Greenbelt, Maryland, USA.

³Department of Terrestrial Magnetism, Carnegie Institution of Washington, Washington,
DC, USA.

⁴Lamont-Doherty Earth Observatory, Columbia University, Palisades, New York, USA.

⁵Planetary Science Institute, Tucson, Arizona, USA.

Matthieu Talpe

Email: mtalpe@mit.edu

Phone: 262-337-0213

ABSTRACT

Earth-based radar images of Mercury show radar-bright material inside impact craters near the planet's poles. A previous study indicated that the polar-deposit-hosting craters (PDCs) at Mercury's north pole are shallower than craters that lack such deposits. We use data acquired by the Mercury Laser Altimeter on the MESSENGER spacecraft during 11 months of orbital observations to revisit the depths of craters at high northern latitudes on Mercury. We measured the depth and diameter of 537 craters located poleward of 45°N, evaluated the slopes of the northern and southern walls of 30 PDCs, and assessed the floor roughness of 94 craters, including nine PDCs. We find that the PDCs appear to have a fresher crater morphology than the non-PDCs and that the radar-bright material has no detectable influence on crater depths, wall slopes, or floor roughness. The statistical similarity of crater depth-diameter relations for the PDC and non-PDC populations places an upper limit on the thickness of the radar-bright material (< 170 m for a crater 11 km in diameter) that can be refined by future detailed analysis. Results of the current study are consistent with the view that the radar-bright material constitutes a relatively thin layer emplaced preferentially in comparatively young craters.

TEXT

1. Introduction

Earth-based radar imaging of Mercury dating back two decades revealed that a number of areas near both poles of the planet display high radar reflectivity at 3.5-cm [Butler *et al.*, 1993, 1994] and 12.6-cm wavelengths [Harmon and Slade, 1992; Slade *et al.*, 1992; Harmon *et al.*, 2001] (Figure 1). Images acquired from Mariner 10 flybys in 1974 and 1975 indicated that the locations of many of those radar-bright features are correlated with the interiors of impact craters [Harmon *et al.*, 1994, 2011].

A number of hypotheses have been put forth to explain the source of the radar-bright deposits: volcanic outgassing of volatiles [Butler *et al.*, 1993], production of sodium and water vapor from the chemical sputtering of surface rocks driven by the impact of magnetospheric protons [Potter, 1995], migration and deposition of exogenous volatiles from cometary and meteoroid impacts [Butler, 1997; Killen *et al.*, 1997; Moses *et al.*, 1998], high concentrations of surficial sulfides [Sprague *et al.*, 1995], and decreased dielectric loss in silicate material at the low polar temperatures that characterize the permanently shadowed regions of polar craters [Starukhina, 2001]. In addition, modeling of the thermal environment at the poles indicates that some forms of volatiles (e.g., water ice) could be stable in permanently shadowed regions of polar craters for timescales exceeding 1 Gy [Paige *et al.*, 1992; Ingersoll *et al.*, 1992; Vasavada *et al.*, 1999].

The scientific payload of the MErcury Surface, Space ENvironment, GEochemistry, and Ranging (MESSENGER) spacecraft has made a number of observations relevant to the nature of radar-bright polar deposits since MESSENGER was inserted into orbit

about Mercury on 18 March 2011. These observations include the discovery from MESSENGER's X-Ray Spectrometer (XRS) that Mercury has a high overall surface abundance of sulfur (up to 4 wt%) [Nittler *et al.*, 2011], measurement of generally low reflectivity of radar-bright material at the 1064-nm wavelength of MESSENGER's Mercury Laser Altimeter (MLA) [Neumann *et al.*, 2012], and the demonstration that radar-bright polar deposits coincide with areas of permanent shadow in images acquired by MESSENGER's Mercury Dual Imaging System (MDIS) [Chabot *et al.*, 2012a,b]. Recent updates to thermal models of impact craters at high latitudes also have explored the range of stability of other impact-delivered volatiles, including organic compounds, as well as water ice in polar cold traps [Zhang and Paige, 2009; Paige *et al.*, 2012].

In this paper we use observations from MESSENGER's MLA instrument [Cavanaugh *et al.*, 2007] to address the following two questions: (1) what does a systematic survey of crater morphometry indicate about the north polar region of Mercury, and (2) does the radar-bright material affect the morphology of these polar-deposit-hosting craters (PDCs)?

In an earlier study, the shapes of 170 craters distributed at both poles and some equatorial areas were measured and compared on a regional basis [Barlow *et al.*, 1999]. That study was motivated by similar analysis of Martian craters, which showed that subsurface ice accelerates topographic relaxation, resulting in smaller crater depths at a given crater diameter at higher latitudes [Cintala *et al.*, 1980; Squyres and Carr, 1986]. However, no such regional variation in the relation between crater depth and diameter was detected on Mercury.

A more recent study of the morphometry of 12 PDCs located near Mercury's north pole yielded the conclusion that the mean ratio of crater depth to rim-crest diameter for the PDCs is two-thirds that of the mean ratio for a comparable population of neighboring craters lacking such deposits [Vilas *et al.*, 2005]. One explanation put forward to explain this shallowing is a thick (hundreds of meters) layer of volatiles mixed with non-volatile material overlying the floors of the PDCs; this layer could be composed of dust delivered by the impacts of volatile-rich comets or asteroids [Vilas *et al.*, 2005].

The studies of both Barlow *et al.* [1999] and Vilas *et al.* [2005] involved the application of shadow-length techniques to Mariner 10 images. In those methods, measurements of shadow lengths and knowledge of ephemerides and spacecraft attitude are combined to estimate variations in topographic elevation. In contrast, we use here the geodetically controlled altimetry data acquired by the MLA to assess the geometric properties of craters and avoid the uncertainties of shadow-length techniques.

2. Methods

2.1. From Altimetry to Topography

The MLA is a laser rangefinder that determines topography from pulse-edge timing [Cavanaugh *et al.*, 2007]. The MLA transmits a 1064-nm laser pulse at 8 Hz, illuminating spots that are between 15 m and 100 m in diameter and spaced approximately 400 m apart along the spacecraft ground track [Zuber *et al.*, 2012]. The radial precision of individual measurements is better than 1 m, and the accuracy with respect to Mercury's center of mass is better than 20 m [Smith *et al.*, 2012]. MESSENGER's eccentric orbit during the primary mapping mission (200–500 km

periapsis altitude, 60°N–73°N periapsis latitude, 15,200 km apoapsis altitude, and 12 h period) and MLA instrument specifications (off-nadir observations are limited to slant angles of less than 40° from the vertical and 1000-km range) constrain altimetry coverage to northward of 15°S.

The range of the altimeter from Mercury’s surface is computed from the time of flight of each laser pulse and then converted into an elevation relative to a reference sphere of radius 2440 km from known spacecraft attitude and an orbital position determined from spacecraft radio tracking [Smith *et al.*, 2012]. As of early March 2012, MLA had collected more than 6.2 million altimetry shots and produced a comprehensive topographic map of Mercury’s northern hemisphere [Zuber *et al.*, 2012].

2.2. Crater Selection

For this study we used over 4.25 million altimetry points from MLA’s channel 0, the instrument channel with highest signal-to-noise ratio. The observations were acquired from the time of MESSENGER orbit insertion on 18 March 2011 until mid-February 2012, when the MLA ranging was interrupted due to solar conjunction and to mitigate the thermal stresses incurred during a high-temperature phase of the orbit.

We also used images collected from MESSENGER’s MDIS cameras [Hawkins *et al.*, 2007] to complement altimetry data in selecting craters. The MDIS consists of two cameras: a multi-spectral wide-angle camera and a monochrome narrow-angle camera. MDIS images have been combined into a global mosaic at an average spatial resolution of 250 m per pixel that covers more than 99% of Mercury’s surface [Becker *et al.*, 2012].

The altimetry coverage corresponds to the ground tracks of MLA profiles obtained during nearly 450 orbits. The spacing between each ground track is smallest where the

tracks intersect near 82.5°N (where the latitude equals the orbit inclination) and larger at lower latitudes. Hence, many craters with diameters smaller than the ground track spacing at the lower latitudes are not covered by this altimetry dataset. This latitudinal variation in cross-track coverage introduces a bias in the craters measured in this study, in that craters with the smallest diameters sufficiently well sampled by altimetry are mostly located at higher latitudes. Furthermore, the number of points in MLA's channel 0 decreases in areas with high topographic roughness, e.g., the rims and floors of small craters. The minimum coverage required for a crater to be selected in this study is one crater-centric track (i.e., passing sufficiently close to a crater center to include a representative portion of the crater floor and rims) with good sampling of altimetry on the rims and on the crater floor. The assessment of adequacy of sampling is somewhat qualitative and depends on the topographic coverage, e.g., some craters, with rims and a floor covered by less than 20 MLA shots, are better profiled than other craters covered by more than 50 shots that sample only the rims or unrepresentative portions of the crater floor. Comparison of MDIS images to MLA profile location provides a further basis for the assessment of MLA coverage reliability.

In addition to coverage constraints, we considered a crater's morphologic state. Craters with obliterated rims, infilled floors, embayed features, and/or superposed topographic features were not selected for further analysis on the grounds that their topography is unrepresentative of craters unmodified by such processes.

2.3. Morphometry

We used the geodetically controlled altimetry data provided by MLA to evaluate two standard geometric measures of craters, rim-crest diameter D and crater depth d . We also

assessed the surface roughness of the crater floors over a range of horizontal baselines and evaluated the slopes of poleward- and equator-facing crater walls.

2.3.1. Crater Geometry

The rim-crest diameter D was found by fitting a circle to the crater rims by least squares (Figure 2). The rim crest positions were determined from the two maximum elevations on either side of the crater floor for most crater-centric altimetry profiles. The least squares fit yields a crater center and a diameter with an associated standard deviation.

The crater depth d is defined as the difference in elevation between the rim crest and the floor (Figure 3). The rim crest elevation was taken to be the mean of the highest half of the rim altimetry points, on the grounds that topography-reducing mechanisms are more common than topography-augmenting mechanisms at crater walls. Topography-reducing mechanisms at crater walls are driven by the downward diffusion of landscapes as well as stochastic processes such as the alteration or obliteration of existing rims by subsequent impacts. The altimetry points used in assigning the depth of a floor were selected manually to avoid the bias of superposed craters. The high topographic variability of the rim for some craters (due in part for the crater in Figures 2 and 3 because it overlaps the rim of a larger crater) translates to a large standard deviation for those rim elevation measurements.

Inspection of equivalent MDIS coverage provided corroboration of the MLA-derived measurements and led to the removal from the study of craters with uncharacteristic morphologies or insufficient MLA sampling. In the latter category, for instance, are cases

for which the best-fit circle doesn't follow the physical crater diameter or profiles that sample only the lower crater walls rather than the crater floor.

2.3.2. Crater Floor Roughness

We used a technique that *Kreslavsky and Head* [2000] developed to assess the roughness of the Martian surface. This technique also has been applied to distinguishing terrain types on Mercury from MLA observations [*Yang et al.*, 2011] and on the Moon from measurements made with the Lunar Orbiter Laser Altimeter [*Rosenburg et al.*, 2011].

The roughness at a point on the crater floor R is defined as the absolute value of the differential slope s ,

$$R = \tan^{-1}(s), \quad (1)$$

where the differential slope s is defined as

$$s = |s_L - s_{2L}|, \quad (2)$$

and where s_L and s_{2L} are the slopes of baselines of length L and $2L$, respectively, centered at the point of interest. The slope of each baseline is defined as the slope of the line connecting the two baseline endpoints (Figure 4). For this study, we explored slopes for which L was 0.8, 3.2, or 5.6 km (i.e., $2L$ was 1.6, 6.4, or 11.2 km). Subtracting the longer-baseline slope from the shorter-baseline slope in the expression for differential slope in equation (2) tends to remove the influence of large-scale topographic trends, and calculating the differential slope over several length scales permits an exploration of roughness versus horizontal wavelength. The absolute value operator is applied to the slope difference in equation (2) because a negative differential slope and a positive equivalent contribute similar information to the characterization and comparison of

surface roughness on crater floors. We have taken the roughness for a particular crater floor to be the median value of all the differential slopes for that floor.

2.3.3. Crater Wall Angle

We parameterized the slope of crater walls as a quasi-linear rise in elevation between the base of the wall and the crater rim (Figure 5). Areas of high roughness or surface curvature, such as the rim crests and the transition between the flat crater floor and the wall, were not included in the determination of the crater wall angle. The angle α with respect to the horizontal was defined from the rise in elevation of the wall and the horizontal distance over which that rise can be traced.

We distinguished between north-facing and south-facing walls. *Chabot et al.* [2012b] and *Neumann et al.* [2012] have noted that radar-bright features are primarily found only on or near the southernmost, north-facing crater walls in most craters at high northern latitudes. Therefore, the angles of the northern and southern walls of PDCs were measured separately in order to investigate the possible influence of radar-bright material on wall slopes.

3. Results

3.1. Survey

The depths and diameters were measured for 537 craters that are morphologically fresh and were sufficiently sampled by MLA by mid-February 2012. The latitudinal coverage for these craters extends from 48.7° to 87.8° N (Figure 6), the diameter range spans 1.74 to 207 km, and the depth range spans 0.15 to 4.44 km (Figure 7). Additionally, the floor roughness was measured for 94 of those 537 craters.

3.2. Crater Population Classification

The craters surveyed were classified into four populations on the basis of two categories defined by radar brightness and geological terrain type. This classification facilitates the examination of differences among craters in different target areas as well as any possible influence of polar deposit material on crater morphology.

3.2.1. Radar-bright Deposit

The first category for classification is based on radar brightness. A crater was registered as a PDC if it collocates with a radar-bright feature from the most recently acquired radar image of Mercury's north polar region obtained at the Arecibo Observatory [Harmon *et al.*, 2011]. A total of 42 of the 537 craters are so registered as PDCs (Figure 8a). Most craters poleward of 82°N are PDCs [Chabot *et al.*, 2012b]. Some large radar-bright features within 4° of the north pole were not included in this population because only a few MLA observations collected from off-nadir operation have been obtained of the area northward of 85°N.

3.2.2. Geological Terrain

The second classification category is geological terrain type. The northern volcanic plains (NVP) are a large expanse of smooth plains that occupy the northern lowlands of Mercury, were emplaced shortly after the end of the late heavy bombardment of the inner solar system ~3.8 Ga, and cover more than 6% of Mercury's surface [Head *et al.*, 2011; Yang *et al.*, 2011; Zuber *et al.*, 2012]. Surrounding the NVP is the generally older and more elevated heavily cratered terrain (HCT), a terrain type usually found in close association with intercrater plains [e.g., Spudis and Guest, 1988].

Of the craters characterized in this study, a total of 327 fall within the boundaries of the NVP as defined by *Head et al.* [2011], and 210 are part of the HCT (Figure 8b). The largest craters examined in this study are part of the HCT. In contrast, many of the smaller craters examined are located on the NVP.

4. Interpretation

4.1. Depth Versus Diameter

We first examined the relationship between crater depth and diameter for the different crater populations. The relationship between depth and diameter is a first-order measure of crater morphometry and is commonly used in investigating the processes that affect planetary surfaces [e.g., *Pike*, 1974, 1988; *Garvin et al.*, 2000; *Schenk and Turtle*, 2009].

To quantify the differences among crater populations, we fit a power law to plots of depth versus diameter for subsets of craters from each population. The subsets were chosen on the basis of a diameter range common to all populations as well as morphologic homogeneity.

Crater morphology is influenced by the impactor kinetic energy (in addition to the gravitational acceleration and strength of the target body surface, characteristics expected to be common for the craters in our study) and varies in well-documented ways with crater diameter. The craters in this study range from simple bowl-shaped craters to complex craters with a flat floor, a central peak, and slumped wall terraces [*Melosh*, 1989]. Simple craters tend to have larger ratios of depth to diameter than complex craters, and the change in crater morphology with diameter is manifested as a change in the slope on a log-log plot of depth versus diameter. *Pike* [1988] demonstrated that the

morphologic transition between simple and complex craters on Mercury occurs near a diameter of 10 km. For the data set in this study, the transition diameter is about 8 km as seen by the break in slope in a plot of depth versus diameter (Figure 7).

The four populations of craters in this study all included complex craters, but the HCT lacks PDCs in the simple-crater regime. The non-uniform distribution may be explained by the tendency for radar-bright material to be located near one of Mercury’s “cold poles” at 90°E [Chabot *et al.*, 2012a,b; Paige *et al.*, 2012]. To avoid uneven contributions from simple craters in the different crater populations, the power law fit to plots of depth versus diameter was applied only to the complex craters in each population that have a diameter between 11 and 50 km (Figure 8 and Table 1).

4.1.1. HCT Craters Versus NVP Craters

At a given diameter D , the full population of craters in the HCT has a wider range in depth d than does the comparable population of craters in the NVP (Figure 8). This generalization is also indicated by the larger standard deviation σ of the observed depth d minus the depth d_f predicted by the power-law fits (Table 1).

This dispersion in d can be explained by considering the difference in age of the terrains and the evolution of the cratering flux [Spudis and Guest, 1988]. The emplacement of the northern smooth plains over an older cratered surface is thought to have occurred at ~3.8 Ga. [Head *et al.*, 2011], similar to the time of emplacement of smooth plains within and exterior to the Caloris basin [Strom *et al.*, 2011]. Such a time postdated the pre-Tolstojan [Spudis and Guest, 1988], the epoch during which the impact flux was the highest [Neukum *et al.*, 2001]. In particular, most of the craters on the NVP formed after the end of the late heavy bombardment of the inner solar system [Strom *et*

al., 2011], whereas the surface of the HCT includes the effects of numerous impacts that occurred during the late heavy bombardment [*Strom and Neukum*, 1988].

Processes that acted to modify d included subsequent impacts on or near crater rims, deposition of impact ejecta onto crater floors, and downslope motion of craters walls and central peaks driven by micrometeoroid bombardment, seismic shaking, and other effects [e.g., *Head*, 1975]. The same processes also contribute to enlarging the diameter D , but their effect on D is small compared with that on d .

Because the cumulative effect of modification processes on crater shape increases with the time exposed to impact bombardment, the population of craters in the HCT includes more degraded examples than the population of craters on the NVP. This difference likely accounts for the greater dispersion in d at a given D for the HCT than for the NVP.

4.1.2. PDCs Versus Non-PDCs

We used a statistical tool to test the differences in d/D for samples of PDCs and non-PDCs. The statistical test performed is the Wilcoxon rank-sum test (also known as the Mann-Whitney test), a variant of the Student's- t test applied in comparisons of crater populations by *Barlow et al.* [1999] and *Vilas et al.* [2005]. We selected samples of craters on the basis of a diameter range for which the crater density was similar for the PDC and non-PDC populations (Table 2). The diameter range spanned 10 to 35 km and includes 33 PDCs and 200 non-PDCs. The Wilcoxon rank-sum test provides an assessment of the hypothesis that two samples of unequal sizes come from identical populations without making specific assumptions about the form of the underlying population distribution [*Devore*, 1987]. This test was chosen because the Student's- t test

requires that the samples be normally distributed, which is an invalid assumption for this comparison because the samples fail the χ^2 test at the 95% significance level. The resulting calculated p -value of 0.38 for the Wilcoxon test is outside the rejection region. The rejection region is from 0 to 0.05 for the 95% significance level. The Wilcoxon rank-sum test therefore indicates that the d/D ratios of PDC and non-PDC samples are not statistically different at the 95% significance level. The test would indicate that the samples are statistically different, i.e., by yielding a p -value belonging inside the rejection region between 0 and 0.05, if the d/D values of the 33 PDCs were larger by 0.006 units, which translates to an additional 180 m in depth for a PDC 30 km in diameter and 66 m for a PDC 11 km in diameter, or smaller by 0.015, which translates to a depth lesser by 450 m for a PDC 30 km in diameter and 170 m for a PDC 11 km in diameter.

However, the smaller standard deviation $\sigma_{d/D}$ of d/D ratios for PDCs than for non-PDCs implies that the d/D ratio is more constrained, indicating a less variable morphology. In particular, crater rims for the PDCs are more consistent in their elevation and more nearly circular and concentric to the crater centers (Table 1). Denser MLA coverage at high latitudes could also lead to smaller values of $\sigma_{d/D}$, because for a given range in values used to assess a measurement (e.g., the range in depth values is 0.03 km in Figure 3b), a larger number of points reduces the associated standard variation. However, non-PDCs at similar latitudes have higher $\sigma_{d/D}$ values than PDCs. By arguments similar to those applied above, the lower $\sigma_{d/D}$ for PDCs suggests that crater modification processes operated over less accumulated time than for the population of non-PDCs sampled here. In other words, the PDCs may on average be geologically younger than the non-PDCs at comparable high northern latitudes and therefore have

more favorable illumination conditions for the stability of radar-bright material [*Chabot et al.*, 2012].

4.1.3. Comparison with Previous Work

We compared the morphometry of nine of the 12 PDCs assessed by *Vilas et al.* [2005] with the morphometry determined in this study (Figure 10). The three remaining PDCs are located farther north and are not compared because of insufficient MLA coverage. The diameter values are similar except for craters M2 and L2, which have diameters derived from shadow-length techniques that are substantially larger than the MLA-derived diameters. Large portions of both rims are overlaid with other craters, which may have resulted in a difference in defining the crater rim position and therefore in estimating the diameter between the two studies. The depths of four PDCs from *Vilas et al.* [2005] are smaller than 75% of the equivalent altimetry-derived values, but no systematic error appears to exist, and the inconsistency may be due to the better accuracy and precision of the altimetry-based method. As a result, the depth-to-diameter ratios for seven of the nine PDCs are smaller than those measured by *Vilas et al.* [2005].

Moreover, we may compare power-law fits of depth to diameter with those determined by *Pike* [1988] (Table 3). The exponents in the power law for simple craters are close to 1 for both studies, which corresponds to the well-documented observation that the depths of simple craters are proportional to their diameters by a linear coefficient of about 0.2 [*Pike*, 1974; *Melosh*, 1989]. The linear coefficients are smaller for the depth-diameter relations in this study because a number of degraded (i.e., shallower) craters were included in the fits; the coefficients are close to 0.2 when we confine the fit to data only from the freshest subset of simple craters. The power laws for immature and mature

complex crater regimes have lower exponents than the relations given by *Pike* [1988], i.e., crater depth increases more slowly with increasing diameter. The differences between studies may arise from the differing methodologies for determining depths.

4.2. Other Measurements

We examined the ratios of the slopes of the southward-facing (northern) and northward-facing (southern) walls for 30 PDCs sufficiently well sampled by altimetry. No systematic difference in wall slope was found, as indicated by a mean slope ratio of ~ 1 (Figure 11a). Because radar-bright material tends to be concentrated on northward-facing slopes for craters at high northern latitudes, such material has no detectable effect on wall slope.

Walls are steepest for smaller (< 20 km diameter) complex craters (Figure 11b), which is as expected considering that such craters are closer to the transition diameter from simple to complex craters. In general, slopes are far below the angle of repose predicted for regolith material ($\sim 35^\circ$) [*Van Burkalow*, 1945].

The Wilcoxon rank-sum test was applied to floor roughness values for complex crater floors over three baselines. The calculated p -values for the comparison between the PDC and non-PDC samples at the 0.8-, 3.2- and 5.6-km baselines are 0.234, 0.112 and 0.640 respectively, all above the comparison value of 0.05 for the 95% significance level (i.e., outside the rejection region spanning 0 to 0.05). The test therefore indicates that there is no resolvable difference in roughness between the floors of PDCs and non-PDCs. The median differential slope values and associated standard deviations are somewhat higher for small craters at the largest baseline ($L = 5.6$ km) because the slope measurements

include points for which the footprints sampled the crater wall, which imparted an elevation bias to the slope measurement (Figure 12).

5. Conclusions

Two questions, posed in the introduction, have been addressed in this paper.

What does a systematic survey of crater morphometry indicate about the north polar region of Mercury?

1. The NVP craters have been subjected to less extensive crater modification processes, on average, than HCT craters. The NVP crater population displays a smaller dispersion in d/D values and marginally greater values of d at a given D , and it includes more simple craters sufficiently well preserved to be measured by MLA than does the HCT crater population.

2. PDCs measured in this study appear less degraded, on average, than non-PDCs. The PDCs have a better-preserved morphology (larger d/D) regardless of geographic location than non-PDCs.

3. Radar-bright material is located preferentially in younger craters.

Does the radar-bright material affect the morphology of the polar-deposit-hosting craters?

1. Slopes of crater walls are similar for PDCs in northward-facing and southward-facing directions. Radar-bright material thus has no detectable effect on wall slope.
2. Radar-bright material has no detectable influence on the roughness of the floors of complex craters at the baselines studied (0.8 to 5.6 km).

3. Radar-bright material has no detectable influence on crater morphometry. There is thus no need to invoke thick layers of water ice admixed with non-volatile material, in contrast with the conclusion of *Vilas et al.* [2005]. The inconsistency between the crater morphometry assessed by the two methods does not appear to be systematic and may be due to the higher accuracy and precision of altimetry-derived measurements compared with the topographic information derived from Mariner 10 imaging data.
4. A conservative upper limit on the thickness of radar-bright material on the floors of PDCs is provided by the limiting case of the statistical test used to differentiate the non-PDC and PDC samples (see section 4.1.2.). The current result indicates that the two samples are from a similar population. For the test to yield the result that the PDCs are shallower, at 95% confidence, than the non-PDCs (i.e., for the p -value of the test to fall within the rejection region between 0 and 0.05), the d/D values of the PDC sample would have to be shifted uniformly by -0.015 relative to those of the non-PDC sample. Such a shift translates to rendering the PDCs shallower by 170 m and 450 m for craters 11 and 30 km in diameter respectively. In other words, for an 11-km-diameter PDC, an upper limit on the thickness of the radar-bright material is 170 m. The 1-m vertical precision of the MLA instrument can, in principle, detect height differences two orders of magnitude smaller but the thickness bounds possible with this study are limited by the variations in estimates of depths and diameters of individual craters and by the natural variations in crater dimensions for a given crater population. The determination with multiple MLA profiles of the two-dimensional floor topography for a

number of fresh PDCs and non-PDCs could provide a stronger upper bound on the thickness of radar-bright material than the statistical test applied here.

Acknowledgments. We thank Nadine Barlow, an anonymous reviewer, and Associate Editor Clark Chapman for helpful comments on an earlier version of this manuscript. The MESSENGER project is supported by the NASA Discovery Program under contracts NASW-00002 to the Carnegie Institution of Washington and NAS5-97271 to The Johns Hopkins University Applied Physics Laboratory.

References

- Barlow, N. G., R. A. Allen, and F. Vilas (1999), Mercurian impact craters: Implications for polar ground ice, *Icarus*, *141*, 194–204.
- Becker, K. J., L. A. Weller, K. L. Edmundson, T. L. Becker, M. S. Robinson, A. C. Enns, and S. C. Solomon (2012), Global controlled mosaic of Mercury from MESSENGER orbital images, *Lunar Planet. Sci.*, *43*, Abstract 2654.
- Butler, B. J. (1997), The migration of volatiles on the surfaces of Mercury and the Moon, *J. Geophys. Res.*, *102*, 19,283–19,291.
- Butler, B. J., D. O. Muhleman, and M. A. Slade (1993), Mercury: Full-disk radar images and the detection and stability of ice at the north pole, *J. Geophys. Res.*, *98*, 15,003–15,023.
- Butler, B. J., D. O. Muhleman, and M. A. Slade (1994), VLA/Goldstone 3.5-cm radar observations of Mercury in 1994: South polar and other results, *Bull. Am. Astron. Soc.*, *26*, 1106.
- Cavanaugh, J. F., et al. (2007), The Mercury Laser Altimeter instrument for the MESSENGER mission, *Space Sci. Rev.*, *131*, 451–479, doi:10.1007/s11214-007-9273-4.
- Chabot, N. L., C. M. Ernst, B. W. Denevi, J. K. Harmon, S. L. Murchie, D. T. Blewett, S. C. Solomon, and E. Zhong (2012a), Areas of permanent shadow in Mercury's south polar region ascertained by MESSENGER orbital imaging, *Geophys. Res. Lett.*, *39*, L09204, doi:10.1029/2012GL051526.

- Chabot, N. L., C. M. Ernst, J. K. Harmon, S. L. Murchie, S. C. Solomon, D. T. Blewett, and B. W. Denevi, Craters hosting radar-bright deposits in Mercury's north polar region: Areas of persistent shadow determined from MESSENGER images, submitted to *JGR-Planets*, 2012b.
- Cintala, M. J., and P. J. Mouginis-Mark (1980), Martian fresh crater depths: More evidence for subsurface volatiles?, *Geophys. Res. Lett.*, 7, 329–332.
- Devore, J. L. (1987), *Probability and Statistics for Engineering and the Sciences*, Brooks/Cole, Monterey, Calif., pp. 525-529.
- Garvin, J. B., S. E. H. Sakimoto, J. J. Frawley, and C. Schnetzler (2000), North polar region craterforms on Mars: Geometric characteristics from the Mars Orbiter Laser Altimeter, *Icarus*, 144, 329–352, doi:10.1006/icar.1999.6298.
- Harmon, J. K., and M. A. Slade (1992), Radar mapping of Mercury: Full-disk delay–Doppler images, *Science*, 258, 640–643.
- Harmon, J. K., M. A. Slade, R. A. Vélez, A. Crespo, M. J. Dryer, and J. M. Johnson (1994), Radar mapping of Mercury's polar anomalies, *Nature*, 369, 213–215.
- Harmon, J. K., P. J. Perillat, and M. A. Slade (2001), High-resolution radar imaging of Mercury's north pole, *Icarus*, 149, 1–15.
- Harmon, J. K., M. A. Slade, and M. S. Rice (2011), Radar imagery of Mercury's putative polar ice: 1999-2005 Arecibo results, *Icarus*, 211, 37–50, doi:10.1016/j.icarus.2010.08.007.
- Hawkins, S. E., III, et al. (2007), The Mercury Dual Imaging System on the MESSENGER spacecraft, *Space Sci. Rev.*, 131, 247–338, doi:10.1007/s11214-007-9266-3.

- Head, J. W., III (1975), Processes of lunar crater degradation: Changes in style with geologic time, *Moon*, *12*, 299–329.
- Head, J. W., et al. (2011), Flood volcanism in the northern high latitudes of Mercury revealed by MESSENGER, *Science*, *333*, 1853–1856.
- Killen, R. M., J. Benkhoff, and T. H. Morgan (1997), Mercury’s polar caps and the generation of an OH exosphere, *Icarus*, *125*, 195–211.
- Kreslavsky, M. A., and J. W. Head III (2000), Kilometer-scale roughness of Mars: Results from MOLA data analysis, *J. Geophys. Res.*, *105*, 26,695–26,711, doi:10.1029/2000JE001259.
- Ingersoll, A. P., T. Svitek, and B. C. Murray (1992), Stability of polar frosts in spherical bowl-shaped craters on the Moon, Mercury, and Mars, *Icarus*, *100*, 40–47.
- Melosh, H. J. (1989), *Impact Cratering: A Geologic Process*, Oxford University Press, New York, pp. 14-21.
- Moses, J. I., K. Rawlins, K. Zahnle, and L. Dones (1998), External sources of water for Mercury’s putative ice deposits, *Icarus*, *137*, 197–221.
- Neukum, G., J. Oberst, H. Hoffman, R. Wagner, and B. A. Ivanov (2001), Geologic evolution and cratering history of Mercury, *Planet. Space Sci.*, *49*, 1507–1521.
- Neumann, G. A., J. F. Cavanaugh, X. Sun, E. Mazarico, D. E. Smith, M. T. Zuber, S. C. Solomon, and D. A. Paige (2012), Dark material at the surface of polar crater deposits on Mercury, *Lunar Planet. Sci.*, *43*, Abstract 2651.
- Nittler, L. R., et al. (2011), The major-element composition of Mercury’s surface from MESSENGER X-ray spectrometry, *Science*, *333*, 1847–1849, doi:10.1126/science.1211567.

- Paige, D. A., S. E. Wood, and A. R. Vasavada (1992), The thermal stability of water ice at the poles of Mercury, *Science*, 258, 643–646, doi:10.1126/science.258.5082.643.
- Paige, D. A., M. A. Siegler, J. K. Harmon, D. E. Smith, M. T. Zuber, G. A. Neumann, and S. C. Solomon (2012), Thermal stability of frozen volatiles in the north polar region of Mercury, *Lunar Planet. Sci*, 43, Abstract 2875.
- Pike, R. J. (1974), Depth/diameter relations of fresh lunar craters: Revision from spacecraft data, *Geophys. Res. Lett.*, 1, 291-294.
- Pike, R. J. (1988), Geomorphology of impact craters on Mercury, in *Mercury*, edited by F. Vilas, C. R. Chapman, and M. S. Matthews, pp. 165–273, University of Arizona Press, Tucson, Ariz.
- Potter, A. E. (1995), Chemical sputtering could produce sodium vapor and ice on Mercury, *Geophys. Res. Lett.*, 22, 3289–3292.
- Rosenburg, M. A., O. Aharonson, J. W. Head, M. A. Kreslavsky, E. Mazarico, G. A. Neumann, D. E. Smith, M. H. Torrence, and M. T. Zuber (2011), Global surface slopes and roughness of the Moon from the Lunar Orbiter Laser Altimeter, *J. Geophys. Res.*, 116, E02001, doi:10.1029/2010JE003716.
- Schenk, P. M., and E. P. Turtle (2009), Europa’s impact craters: Probes of the icy shell, in *Europa*, edited by R. T. Pappalardo, W. B. McKinnon, and K. Khurana, pp. 180–198, University of Arizona Press, Tucson, Ariz.
- Slade, M. A., B. J. Butler, and D. O. Muhleman (1992), Mercury radar imaging: Evidence for polar ice, *Science*, 258, 635–640.
- Smith, D. E., et al. (2012), Gravity field and internal structure of Mercury from MESSENGER, *Science*, 336, 214–217, doi:10.1126/science.1218809.

- Sprague, A. L., D. M. Hunten, and K. Lodders (1995), Sulfur at Mercury, elemental at the poles and sulfides in the regolith, *Icarus*, *118*, 211–215.
- Spudis, P. D., and J. E. Guest (1988), Stratigraphy and geologic history of Mercury, in *Mercury*, edited by F. Vilas, C. R. Chapman, and M. S. Matthews, pp. 118–164, University of Arizona Press, Tucson, Ariz.
- Squyres, S. W., and M. H. Carr (1986), Geomorphic evidence for the distribution of ground ice on Mars, *Science*, *231*, 249–252.
- Strom, R. G., and G. Neukum (1988), The cratering record on Mercury and the origin of impacting objects, in *Mercury*, edited by F. Vilas, C. R. Chapman, and M. S. Mathews, pp. 336–373, University of Arizona Press, Tucson, Ariz.
- Strom, R. G., M. E. Banks, C. R. Chapman, C. I. Fassett, J. A. Forde, J. W. Head III, W. J. Merline, L. M. Prockter, and S. C. Solomon (2011), Mercury crater statistics from MESSENGER flybys: Implications for stratigraphy and resurfacing history, *Planet. Space Sci.*, *59*, 1960–1967.
- Starukhina, L. (2001), Water detections on atmosphereless celestial bodies: Alternative explanations of the observations, *J. Geophys. Res.*, *106*, 14,701–14,710.
- Van Burkalow, A. (1945), Angle of repose and angle of sliding friction: An experimental study, *Geol. Soc. Am. Bull.*, *56*, 669–707.
- Vasavada, A. R., D. A. Paige, and S. E. Wood (1999), Near-surface temperature on Mercury and the Moon the stability of polar ice deposits, *Icarus*, *141*, 179–193.
- Vilas, F., P. S. Cobian, N. G. Barlow, and S. M. Lederer (2005), How much material do the radar-bright craters at the Mercurian poles contain?, *Planet. Space Sci.*, *53*, 1496–1500.

- Yang, D., G. A. Neumann, M. T. Zuber, and S. C. Solomon (2011), Distribution of surface slopes and roughness in Mercury's northern hemisphere, Abstract P41A-1577, presented at 2011 Fall Meeting, AGU, San Francisco, Calif., 5–9 Dec.
- Zhang, J. A., and D. A. Paige (2009), Cold-trapped organic compounds at the poles of the Moon and Mercury: Implications for origins, *Geophys. Res. Lett.*, *36*, L16203, doi:10.1029/2009GL038614.
- Zuber, M. T., et al. (2012), Topography of the northern hemisphere of Mercury from MESSENGER laser altimetry, *Science*, *336*, 217–220, doi:10.1126/science.1218805.

FIGURE CAPTIONS

Figure 1. Stereographic projection of Mercury’s north polar region. The bright areas correspond to radar-bright material and collocate polar craters. Figure 4 in *Harmon et al.* [2011].

Figure 2. Illustration of the method used to determine crater diameter. (a) Image of a complex 33-km-diameter crater centered at 83°N , 208°E ; the image is a portion of the MDIS global mosaic. This crater, given the informal name K2 [*Vilas et al.*, 2005], hosts polar deposits described as “weak [bright] features” on page 7 of *Harmon et al.* [2001]. (b) Plan view with overlaid MLA tracks, color-coded by elevation. (c) The crater rim-crest positions, designated by the green stars, are determined from the highest elevations in the vicinity of the imaged rim. (d) The rim-crest diameter is computed from a least-squares fit of a circle (thick red line) to rim locations. The crater center position is indicated by the plus sign, and \pm one standard deviations ($\pm 1\sigma$) from the crater diameter are denoted by the two thin red circles.

Figure 3. Illustration of the method used to determine crater depth. (a) Plan view of the crater in Figure 2 with a near-center-crossing MLA profile overlaid. (b) Topographic cross-section along the selected MLA profile. Thick red lines denote the measured elevations of the rim and floor and $\pm 1\sigma$ are denoted by the thin red lines.

Figure 4. Illustration of the measurement of slope s_L over a baseline of length $L = 3.2$ km at a given point (blue circle) along a hypothetical topographic profile for which successive observation points (red circles) are separated by 400 m. The yellow lines represent the slope between the extremities of the baselines of length L and $2L$.

Figure 5. Illustration of the measurement of crater wall slope. (a) MLA coverage of an unnamed polar-deposit-hosting complex crater 32 km in diameter centered at 79.3°N, 38.9°E. The black lines outline the north-south band selected for determination of wall slopes. (b) Interpolated MLA coverage color-coded for elevation. Distances are with respect to the crater center. (c) Downslope portions of the northern and southern crater walls for which the slope α is determined.

Figure 6. Locations of the 537 craters characterized in this study in a polar stereographic projection about Mercury's north pole.

Figure 7. Depth versus diameter for the 537 craters characterized in this study. The crater diameter at which craters tend to transition in morphological form between simple and complex craters with increasing diameter is indicated by the dashed line at 8 km diameter.

Figure 8. The craters of this study divided by two classification schemes in two polar stereographic projections. (a) The first classification criterion is whether a crater is a polar-deposit-hosting crater (PDC) as resolved in the most recent Earth-based radar

images of the region [Harmon *et al.*, 2011]. (b) The second classification criterion is whether a crater lies within Mercury's northern volcanic plains (NVP) or in older heavily cratered terrain (HCT).

Figure 9. Depth versus diameter for the four different crater populations in this study. The thick lines denote power law fits to the data points for complex craters between 11 and 50 km in diameter; $\pm 1\sigma$ are denoted by the dashed lines.

Figure 10. Comparison of crater depths and diameters for the nine PDCs assessed and assigned informal names by Vilas *et al.* [2005] and re-evaluated in this study. (a) Depth-to-diameter values from shadow-length measurements and MLA-derived topography. (b) Ratio of diameter values from shadow-length measurements to those from MLA topography. (c) Ratio of depth values from shadow-length measurements to those from MLA topography.

Figure 11. Wall slope angles versus crater diameter for the 30 PDCs sufficiently well sampled by altimetry data. (a) The ratio of northern wall slope to southern wall slope (N/S ratio). The mean ratio is denoted by the thick horizontal line and $\pm 1\sigma$ is denoted by the thin horizontal lines. (b) Mean wall slope angle versus crater diameter for the same population of PDCs. The mean slope angle is the average of the northern and southern wall slope values; the two slope angles are indicated by the ends of the vertical lines through each mean value.

Figure 12. Absolute value of median differential slope (MDS) for 94 craters sufficiently large to display a generally flat crater floor. The associated $\pm 1\sigma$ are denoted as vertical lines; a number of standard deviations are smaller than the point size and are therefore not visible. The MDS values are shown for three different baseline lengths: L is 0.8, 3.2, and 5.6 km from top to bottom.

TABLES

Table 1. Power-law fits of depth versus diameter for four populations of craters with D between 11 and 50 km.

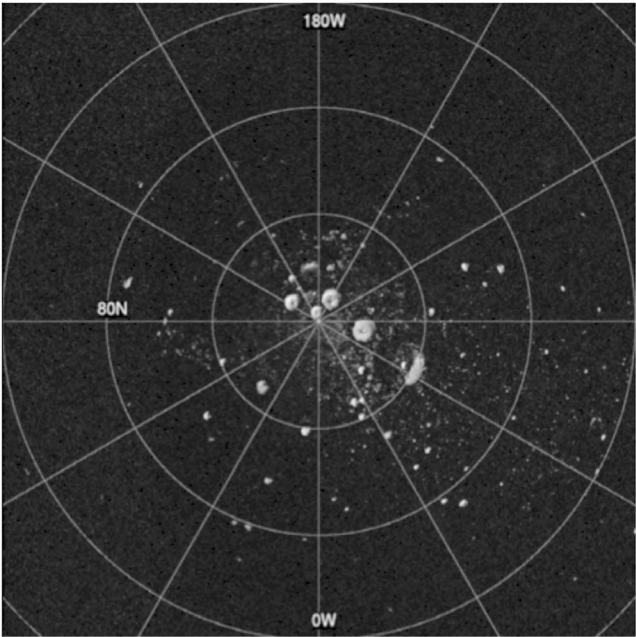
		Non-PDCs	PDCs	Non-PDCs and PDCs
HCT	Crater number n	121	4	125
	Fit depth d_f	$0.84 D^{0.21}$	$1.24 D^{0.16}$	$0.85 D^{0.21}$
	Standard deviation σ of $d - d_f$	0.340	0.026	0.339
	Standard deviation $\sigma_{d/D}$ of d/D	0.035	0.026	0.035
NVP	Crater number n	103	31	134
	Fit depth d_f	$0.66 D^{0.29}$	$0.53 D^{0.39}$	$0.64 D^{0.31}$
	Standard deviation σ of $d - d_f$	0.145	0.171	0.140
	Standard deviation $\sigma_{d/D}$ of d/D	0.029	0.025	0.028
NVP and HCT	Crater number n	224	35	
	Fit depth d_f	$0.77 D^{0.24}$	$0.54 D^{0.39}$	
	Standard deviation σ of $d - d_f$	0.288	0.175	
	Standard deviation $\sigma_{d/D}$ of d/D	0.033	0.025	

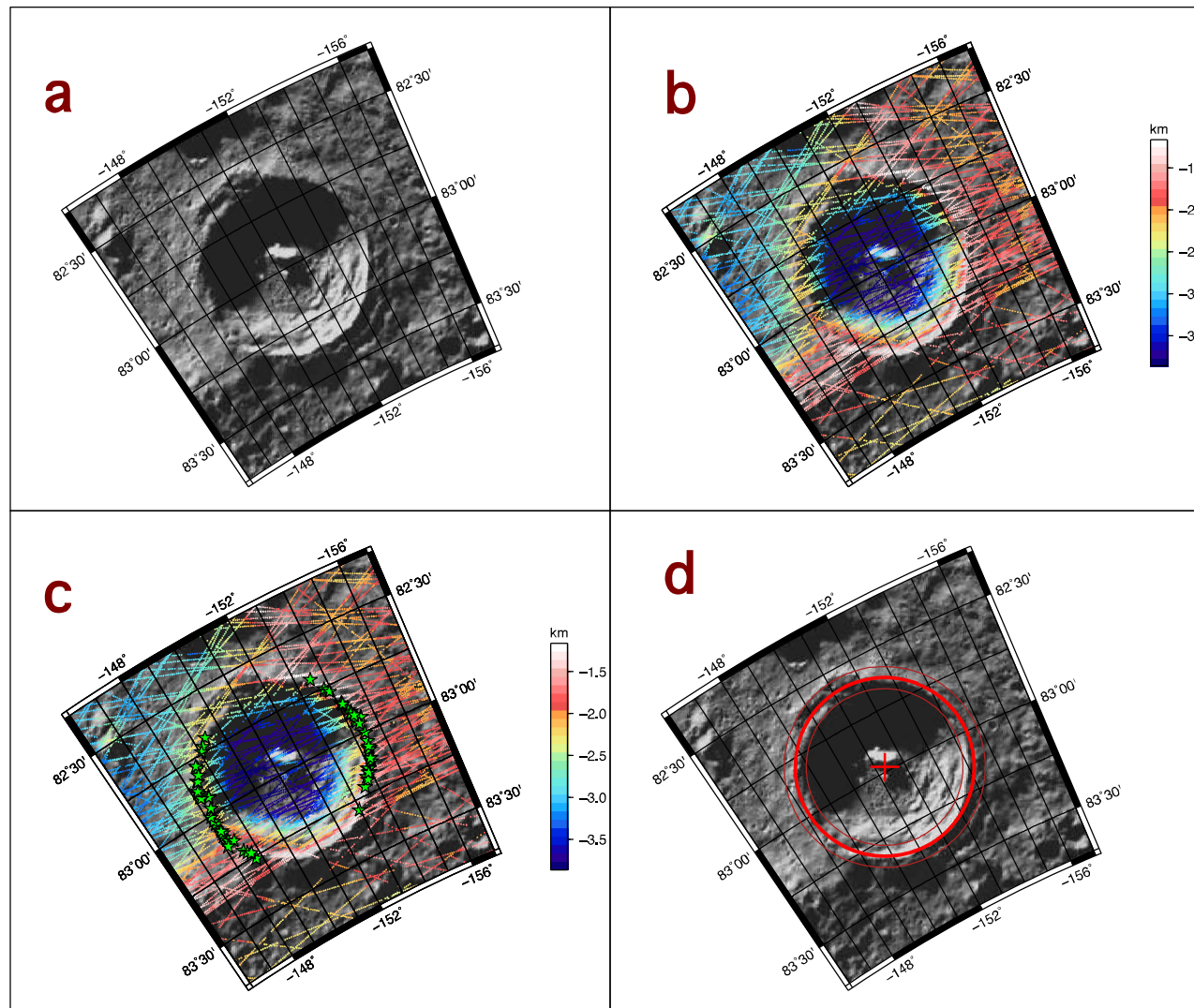
Table 2. Two samples compared in the Wilcoxon rank-sum test.

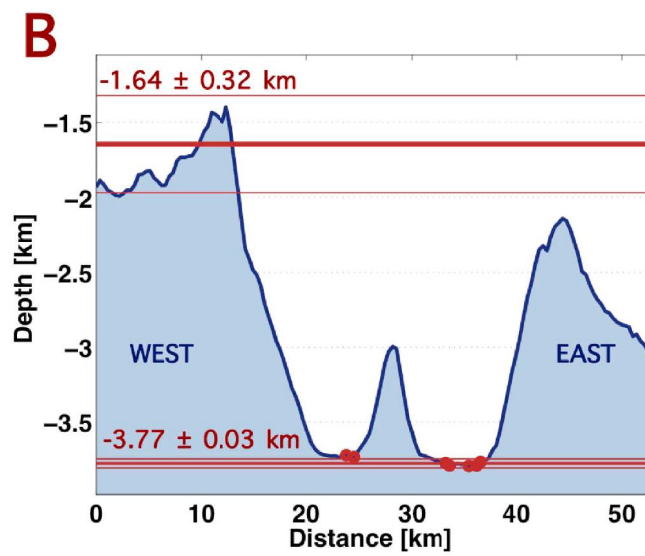
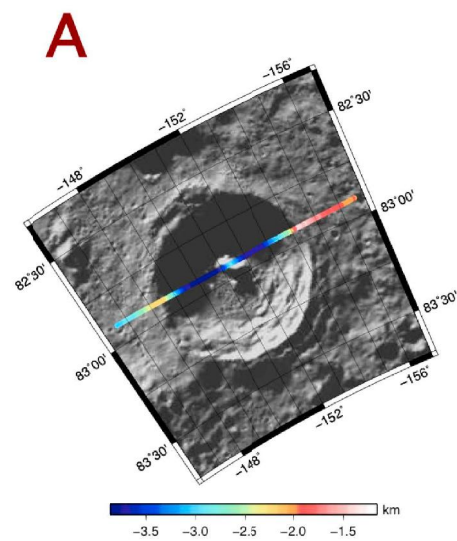
Crater type	Number of craters	d/D
PDCs	33	0.0950 ± 0.026
non-PDCs	200	0.091 ± 0.033

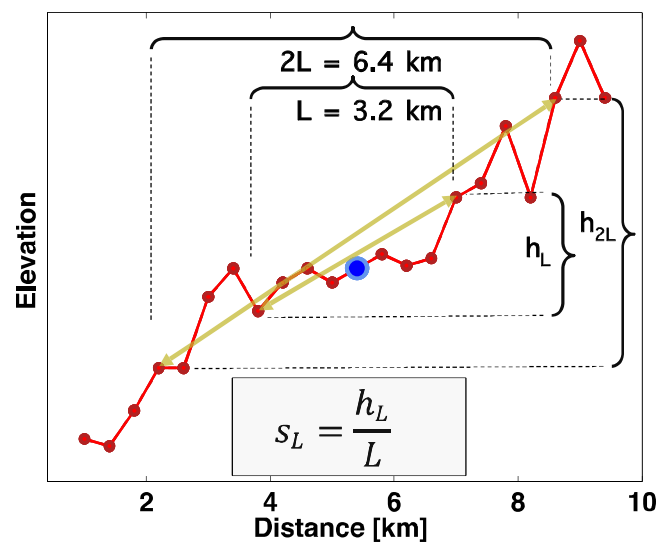
Table 3. Power-law fits for four crater morphological types defined by *Pike* [1988].

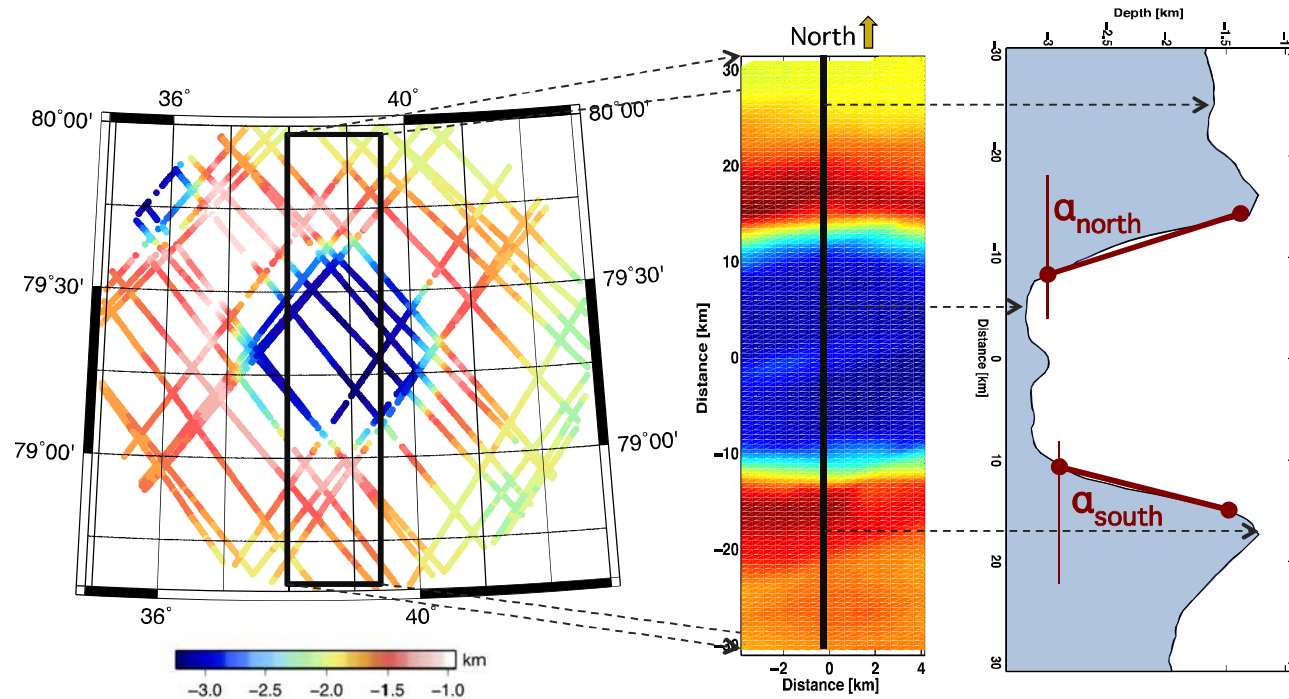
Regime	Diameter range	Fits from <i>Pike</i> [1988]	Fits from this study
Simple (p. 191 in <i>Pike</i> [1988])	225 m – 14.4 km	$d = 0.199 D^{0.995}$	$d = 0.138 D^{0.970}$
Modified-simple (p.197)	4.6 km – 12.7 km	$d = 0.151 D^{1.029}$	$d = 0.145 D^{0.967}$
Immature-complex (p. 198)	9.5 km – 29 km	$d = 0.410 D^{0.490}$	$d = 0.829 D^{0.212}$
Mature-complex (p. 206)	30 km – 175 km	$d = 0.353 D^{0.496}$	$d = 0.712 D^{0.277}$











a

b

c

